AGU PUBLICATIONS

JGR

Journal of Geophysical Research: Solid Earth

RESEARCH ARTICLE
10.1002/2013JB010676

Key Points:
- Shear wave splitting measurements are made on and offshore South Island, NZ
- Strong anisotropy spans a zone 100-200 km on each side of Alpine fault
- Both thin viscous sheet and asthenospheric models match observed anisotropy

Correspondence to:
D. W. Zietlow,
daniel.zietlow@colorado.edu

Citation:
Zietlow, D. W., A. F. Sheehan, P. H. Molnar, M. K. Savage, G. Hirth, J. A. Collins, and B. H. Hager (2014), Upper mantle seismic anisotropy at a strike-slip boundary: South Island, New Zealand, *J. Geophys. Res. Solid Earth*, *119*, 1020–1040, doi:10.1002/2013JB010676.

Received 6 SEP 2013
Accepted 20 DEC 2013
Accepted article online 28 DEC 2013
Published online 5 FEB 2014

Upper mantle seismic anisotropy at a strike-slip boundary: South Island, New Zealand

Daniel W. Zietlow[1], Anne F. Sheehan[1], Peter H. Molnar[1], Martha K. Savage[2], Greg Hirth[3], John A. Collins[4], and Bradford H. Hager[5]

[1]CIRES and Department of Geological Sciences, University of Colorado Boulder, Boulder, Colorado, USA, [2]Institute of Geophysics, Victoria University of Wellington, Wellington, New Zealand, [3]Department of Geological Sciences, Brown University, Providence, Rhode Island, USA, [4]Department of Geology and Geophysics, Woods Hole Oceanographic Institution, Woods Hole, Massachusetts, USA, [5]Department of Earth, Atmospheric and Planetary Sciences, Massachusetts Institute of Technology, Cambridge, Massachusetts, USA

Abstract New shear wave splitting measurements made from stations onshore and offshore the South Island of New Zealand show a zone of anisotropy 100–200 km wide. Measurements in central South Island and up to approximately 100 km offshore from the west coast yield orientations of the fast quasi-shear wave nearly parallel to relative plate motion, with increased obliquity to this orientation observed farther from shore. On the eastern side of the island, fast orientations rotate counterclockwise to become nearly perpendicular to the orientation of relative plate motion approximately 200 km off the east coast. Uniform delay times between the fast and slow quasi-shear waves of nearly 2.0 s onshore continue to stations approximately 100 km off the west coast, after which they decrease to ~1 s at 200 km. Stations more than ~300 km from the west coast show little to no splitting. East coast stations have delay times around 1 s. Simple strain fields calculated from a thin viscous sheet model (representing distributed lithospheric deformation) with strain rates decreasing exponentially to both the northwest and southeast with *e*-folding dimensions of 25–35 km (approximately 75% of the deformation within a zone 100–140 km wide) match orientations and amounts of observed splitting. A model of deformation localized in the lithosphere and then spreading out in the asthenosphere also yields predictions consistent with observed splitting if, at depths of 100–130 km below the lithosphere, typical grain sizes are ~ 6–7 mm.

1. Introduction

Measurements of seismic anisotropy arguably offer the best way to constrain deformation deep in the Earth's subsurface [e.g., *Silver*, 1996]. With such measurements, it becomes possible to describe the distribution of strain in the mantle lithosphere (used here to include the relatively strong layer at temperatures less than around 1200°C), as well as the underlying asthenosphere, in active tectonic regions such as strike-slip zones. Specifically, does the lithosphere deform continuously over a broad region on the order of hundreds of kilometers, or is lithospheric deformation localized within a few kilometers around a fault that penetrates the lithosphere, with more diffuse shear spreading out within the underlying asthenosphere?

The South Island of New Zealand offers an ideal location to investigate subsurface deformation in a strike-slip zone. The tectonic history of the region is known and relatively simple (Figure 1). Plate reconstructions indicate ~850 km of displacement between the plates over the past 45 Ma [*Sutherland*, 1999; *Cande and Stock*, 2004]. The Alpine fault, a predominately dextral strike-slip fault running the length of the South Island and the major tectonic feature of the central portion of the South Island, has accommodated approximately 460 km of this displacement since 45 Ma [e.g., *Sutherland et al.*, 2000]. Over this time period, the relative motion between the Australian and Pacific plates changed little, though a component of convergence initiated around 11 Ma [*Cande and Stock*, 2004]. This convergence resulted in approximately 100 km of shortening across the South Island [*Walcott*, 1998] and the creation of the Southern Alps. Today, geodetic measurements show that the present plate motion is resolved into approximately 36–39 mm/yr parallel and between 9 and 12 mm/yr perpendicular to the Southern Alps [*Beavan et al.*, 1999].

Within the South Island, the style of deformation varies from north to south. Northeast of the South Island, westward subduction of the Pacific plate beneath the Australian plate occurs at the Hikurangi Trough, becoming increasingly oblique toward the south. This oblique convergence continues under the northern

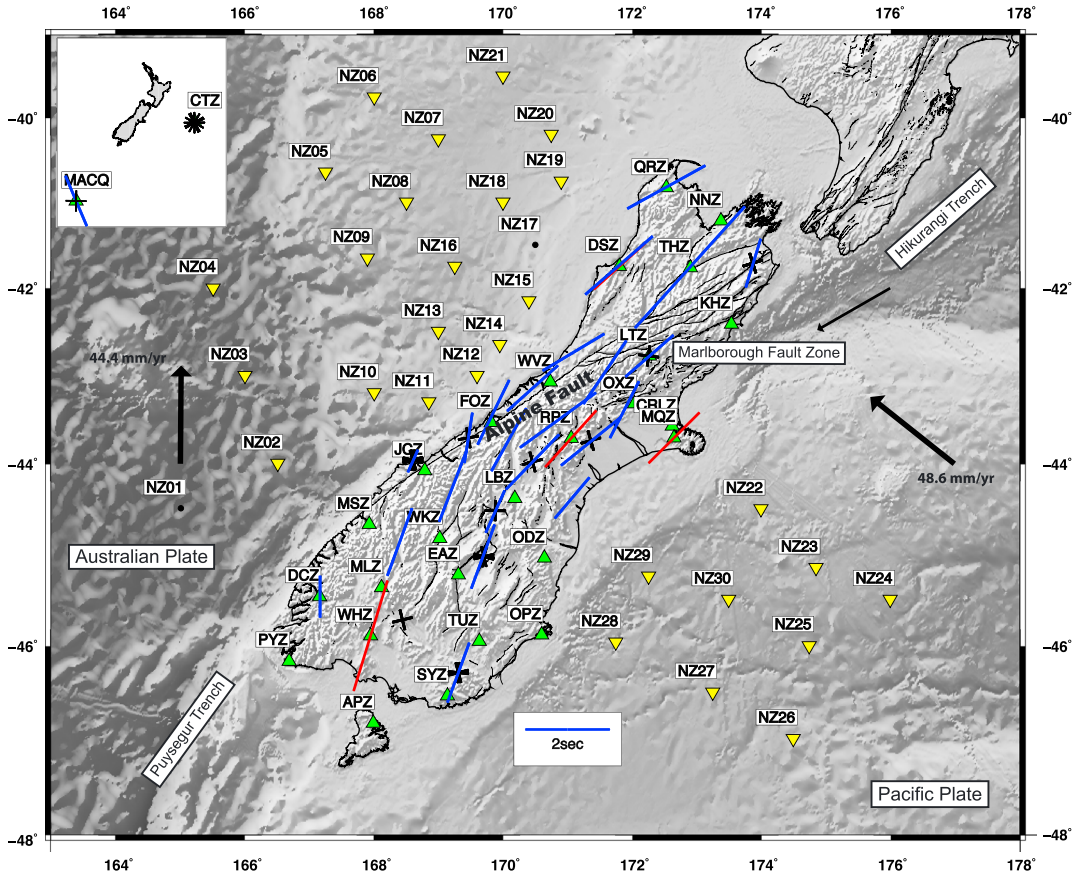

Figure 1. Map of New Zealand and surrounding region showing the location of major tectonic features. Also shown is a summary of previous teleseismic *SKS* splitting measurements made by *Klosko et al.* [1999] (blue bars) and by *Duclos et al.* [2005] (red bars). Black crosses indicate null measurements, with the orientation showing the two possible fast orientations. Lines through stations show orientations of polarization of the faster quasi-shear waves. Lengths of lines are proportional to delay times. Inverted yellow triangles represent the locations of ocean bottom seismometers deployed in the MOANA experiment, and green triangles represent the stations of the New Zealand National Seismograph Network used in this study. Thick black arrows show current absolute plate motion of the Pacific and Australian plates in a hotspot reference frame with no net rotation [*Gripp and Gordon*, 2002]. The thin black arrow shows motion of the Pacific plate relative to the Australian plate averaged over 20 Ma.

portion of the South Island beneath the Marlborough Fault Zone. Here four major strike-slip faults accommodate much of the motion: the Wairau, the Awatere, the Clarence, and the Hope faults [e.g., *Wallace et al.*, 2007]. At the southern end of the Marlborough Fault Zone, slip transfers to the Alpine fault, which accommodates 70–75% of plate motion between the Pacific and Australian plates [*Norris and Cooper*, 2001]. The Alpine fault extends southward into Fiordland where the Australian plate subducts beneath the Pacific plate at the Puysegur Trench and beneath Fiordland.

Previous studies of *SKS* phases found that the mantle underlying the South Island of New Zealand is highly anisotropic (Figure 1) [*Klosko et al.*, 1999; *Duclos et al.*, 2005]. Central portions of the South Island, as well as its northern end, exhibit orientations of fast quasi-shear waves nearly parallel to the trend of the Southern Alps. These regions also exhibit large delay times between fast and slow quasi-shear waves, ranging between 1 and 2 s. The southernmost regions of the island show orientations of the fast quasi-shear wave rotated approximately 20° counterclockwise from those measurements in the northern portion of the island, though delay times remain between 1 and 2 s. Shear wave splitting measurements made on both the Chatham Islands and Macquarie Island (both lying roughly 1000 km from the South Island) exhibit different orientations and amounts of anisotropy from what is observed on the South Island. All measurements made on the Chatham Islands yield nulls, suggesting isotropy. Those from Macquarie Island show a NW fast axis orientation with a delay time of over 1 s [*Klosko et al.*, 1999]. These results suggest that the observed anisotropy in the mantle under the South Island is not due either to older structures found throughout the South Island, as

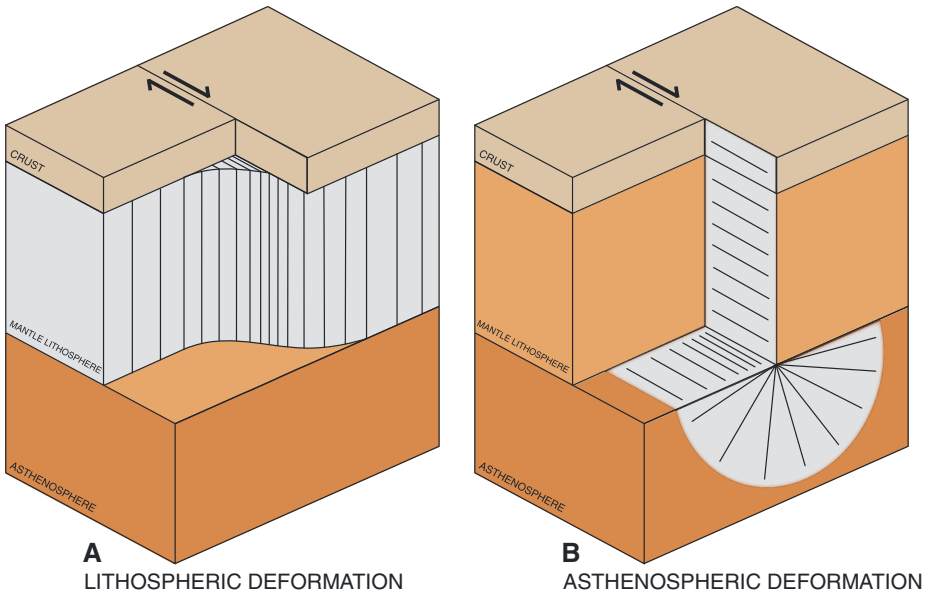

Figure 2. Cartoons showing the proposed mechanisms of deformation, traversing the South Island perpendicular to the Alpine fault. Light areas represent regions deforming via dislocation creep, thus producing a lattice-preferred orientation. (a) A model with a weak lower crust and strong mantle lithosphere in which dislocation creep occurs as in a thin viscous sheet. (b) A model with a strong lithosphere such that localized strain and lattice-preferred orientation develops in the asthenosphere in a region fanning out from the base of the lithosphere.

suggested by *Furlong* [2007], or to absolute plate motion of the Pacific or Australian plates [*Klosko et al*., 1999], as is observed at the East Pacific Rise [*Wolfe and Solomon*, 1998]. Studies of shear wave splitting of *S* arrivals from local earthquakes in the subduction zones yield much smaller delay times than those of *SKS* phases, but it has been difficult to determine whether the smaller values are caused by low anisotropy in the mantle lithosphere or by frequency-dependent splitting [*Audoine et al*., 2000; *Karalliyadda and Savage*, 2013].

Two explanations for the observed pattern of anisotropy have been proposed (Figure 2). In one, anisotropy is caused by shear within the mantle lithosphere across a broad zone that spans the width of the South Island, if not wider [*Molnar et al*., 1999; *Little et al*., 2002; *Moore et al*., 2002], an interpretation invoked in other strike-slip regions [e.g., *Vauchez and Nicolas*, 1991]. GPS studies also suggest that, at least for central portions of the South Island, simple shear likely occurs over a zone approximately 200 km wide [e.g., *Houlié and Stern*, 2012]. Others have inferred that localized deformation in the shallow lithosphere around the Alpine fault continues through the lithosphere into the asthenosphere so that the source of the anisotropy extends to depths of 250 km or more [*Klosko et al*., 1999; *Karalliyadda and Savage*, 2013]. Both interpretations rely on data recorded only by stations deployed across the South Island of New Zealand. As the maximum width of the South Island is approximately 200 km, this limits the lateral extent of the array aperture. Thus, to test these proposed mechanisms of deformation, we devised an experiment that expanded the array aperture.

2. The Marine Observations of Anisotropy Near Aotearoa Experiment

The Marine Observations of Anisotropy Near Aotearoa (MOANA) experiment included a 1 year deployment of ocean bottom seismometers (OBSs) installed off both coasts of the South Island of New Zealand from late January 2009 to early February 2010 (Figure 1). Deployed with approximately 100 km spacing, this array of OBSs increased the aperture of study to 5 times the width of the South Island. Stations NZ01–NZ04 rested on oceanic crust, with the others lying on the continental shelf surrounding New Zealand. All instruments recorded continuously at a sample rate of 50 Hz. These OBSs complemented the existing land stations of the New Zealand National Seismograph Network maintained by GeoNet. All but one of the OBSs (station NZ14) were equipped with Trillium 240 seismometers with the final OBS equipped with a Trillium 40 seismometer. The former are broadband instruments with flat frequency responses between 240 s and 35 Hz. The latter is an intermediate period instrument with a long-period corner at 40 s. Although 30 instruments were deployed, one did not yield usable seismograms (station NZ01), and one was never recovered (station NZ17).

We used Rayleigh wave polarizations to orient the horizontal components of the OBSs [*Stachnik et al*., 2012]. This technique exploits the elliptical particle motion of Rayleigh waves and the fact that this motion is theoretically observed only on the vertical and radial components of ground motion. Since linearity is easier to assess than ellipticity, *Stachnik et al*. [2012] determined instrument orientation by cross correlating the vertical component with the Hilbert transformed radial component. The polarization analysis included first predicting the arrival time of the Rayleigh wave with a group speed of 4.0 km/s and then applying a band-pass filter from 0.02 to 0.04 Hz to the waveform in the window 20 s before and 600 s after this phase arrival. The Hilbert transformed radial components for a range of back azimuths (0°–360°) were cross correlated with the vertical components. The sensor orientation is assumed to correspond to the azimuth of maximum correlation. For the OBSs associated with the MOANA experiment, between 10 and 31 events were used to determine the orientations of the horizontal components.

3. Mantle Anisotropy and Shear Wave Splitting Methods

Within a single anisotropic layer, a traveling shear wave splits into two, orthogonal quasi-shear waves that propagate through the medium with different wave speeds, resulting in two distinct arrivals on a seismogram [*Babuška and Cara*, 1991, and references therein]. Shear wave splitting analyses yield measurements of both the delay time between the fast and slow quasi-shear waves (δt) and the orientation (φ) of the faster quasi-shear wave. These parameters provide information on the orientation and degree of anisotropy within the medium of interest.

In the upper mantle, anisotropy is dominantly a result of lattice-preferred orientation (LPO) or the preferential alignment of crystalline structure in response to finite strain [e.g., *Silver*, 1996; *Savage*, 1999]. Anisotropy is commonly quantified as a percentage: $100(v_{max} - v_{min})/v_{avg}$, where v_{max} is the speed of the fast quasi-shear wave, v_{min} is that of the slow quasi-shear wave, and v_{avg} is the average of the two. It is typically thought that olivine is the principal mineral involved in upper mantle anisotropy, for which percent anisotropy can reach 18% for single crystals, though crystals not aligned in the same direction yield a smaller overall percent anisotropy. Other minerals such as orthopyroxene also contribute [e.g., *Kumazawa*, 1969; *Ribe*, 1992; *Long and Becker*, 2010; *Skemer et al*., 2012]. Deformation in the upper mantle occurs via either diffusion creep or dislocation creep [e.g., *Karato and Wu*, 1993]. Diffusion creep involves the diffusion of atoms along grain boundaries, whereas dislocation creep involves the migration of dislocations in the crystal lattice [*Turcotte and Schubert*, 2002]. In general, only dislocation creep produces the LPO and microstructure consistent with observed anisotropy in the upper mantle [e.g., *Savage*, 1999].

Laboratory experiments suggest that predicted lattice-preferred orientation patterns in olivine aggregates depend on the finite strain [e.g., *Karato et al*., 2008]. At low strain and/or when dynamic recrystallization is limited, the anisotropy of a deformed aggregate can be expressed relative to the principal axes of finite strain. During progressive simple shear (e.g., the Alpine fault), the olivine *a* axes initially orient approximately 45° from the plane of shear and rotate progressively toward that plane as strain accumulates; at sufficiently high strains (>150% in lab samples deformed at 1300°C) and/or cases where dynamic recrystallization is prevalent, the olivine *a* axes rotate to lie within the plane of shear [e.g., *Zhang and Karato*, 1995]. With moderate hydrogen ("water") content (~500 ppm H/Si), such as might be expected in the asthenosphere or within the mantle wedge of a subduction zone, a different pattern of LPO (E-type) is observed [e.g., *Mehl et al*., 2003; *Karato et al*., 2008]. Examination of fabrics in high-temperature shear zones (1000–1200°C) demonstrates that the details of how LPO evolves with progressive simple shear in the Earth match those determined in the lab and that the olivine water content under which the fabric transitions occur is consistent with measurements of water contents preserved in the natural samples [e.g., *Warren et al*., 2008; *Skemer et al*., 2010, 2013]. The agreement between the laboratory and natural observations justifies interpretations of mantle anisotropy guided by the details of the laboratory analyses. Finally, B-type and C-type LPOs observed in lab samples deformed at higher water contents, pressures, and stresses than those required to promote E-type fabric can significantly influence the interpretation of anisotropy [e.g., *Karato et al*., 2008].

To constrain the fast axis orientations and delay times, we employ the method outlined by *Silver and Chan* [1991] as implemented in SplitLab [*Wüstefeld et al*., 2008]. This is a grid search-based method that determines the best fitting splitting parameters (φ and δt) by minimizing energy on the transverse component after removing effects due to shear wave splitting. We also adopt the multiple event splitting method of *Wolfe and*

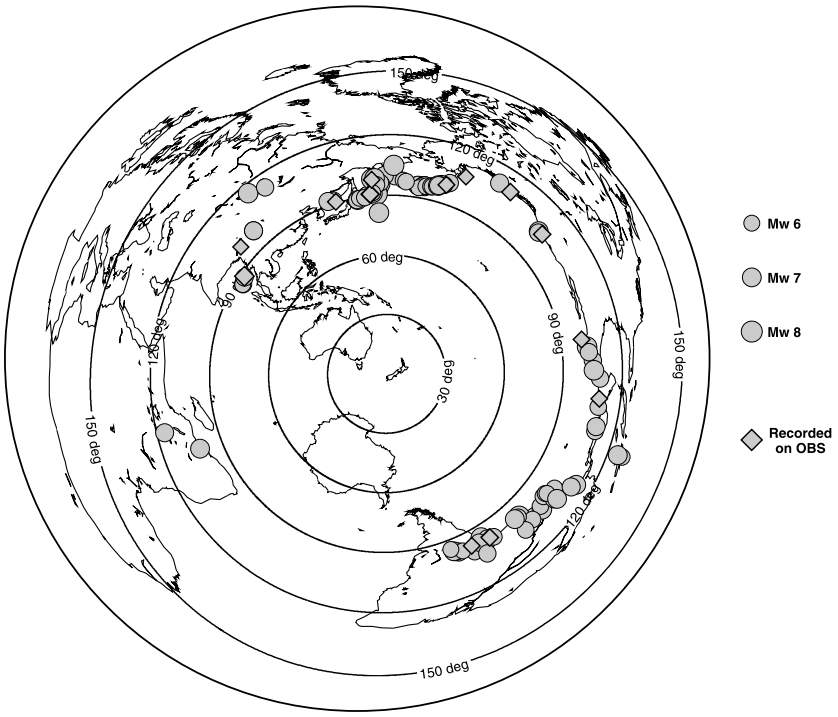

Figure 3. Locations of earthquakes used in this study. All events shown yielded at least one usable measurement. Circles represent events used to constrain splitting parameters only on land stations. Diamonds represent events recorded on both land and ocean bottom seismometers.

Silver [1998] in which the resulting energy contours of individual measurements are stacked. This helps reduce effects of acknowledged shortcomings of *Silver and Chan*'s method in which large amounts of noise and/or small degrees of birefringence can yield incorrect values of φ and δt [*Restivo and Helffrich*, 1999; *Levin et al*., 2007; *Monteiller and Chevrot*, 2010]. In such instances, the measured value of φ lies parallel to the back azimuth of the earthquake used in the analysis, with the result that *Silver and Chan*'s method can yield unrealistically large values of δt. Such measurements are typically classified as null measurements. Because the ocean is inherently a noisy environment, many splitting measurements exhibited these characteristics, which makes it difficult to distinguish null measurements from cases with low signal-to-noise ratios (defined as the ratio of the maximum amplitude on the radial component to the standard deviation of the transverse component in the analysis window). With the stacking method of *Wolfe and Silver* [1998], however, we were able to use such measurements to distinguish noisy waveforms and/or small delay times from nodal results.

4. Results

We examine all *SKS*, *SKKS*, and *PKS* arrivals from earthquakes with magnitude $M_w \geq 5.0$ recorded across the MOANA array between early 2009 and early 2010, as well as by the New Zealand National Seismograph Network between 2003 and April 2012, which included 28 stations on the South Island, Stewart Island, and the Chatham Islands. Since the last major study of *SKS* phases in New Zealand [*Duclos et al*., 2005], several new stations were added to the network, and we could also use more than 8 years of new waveform data from those previously characterized stations. Although we analyzed earthquakes of magnitude $M_w \geq 5.0$ occurring at epicentral distances between 85° and 130° from the South Island, we found all useable events to be of magnitude $M_w > 6.0$ with epicentral distances between 90° and 120°. All the useable phase arrivals were *SKS*, with one useable *SKKS* arrival. The majority of the events occurred in the Aleutian, Kuril, and Peru-Chile subduction zones, resulting in nonuniform back azimuthal coverage, especially on the OBSs (Figure 3 and Table 1). This nonuniform back azimuthal coverage on the OBSs means that we cannot resolve any possible two-layer anisotropy [*Silver and Savage*, 1994].

Table 1. List of Earthquakes Used in This Study[a]

Year	Julian Day	Latitude (°)	Longitude (°)	Depth (km)	M_w	BAZ (°)
2003	022	18.77	−104.1	24	7.5	72.1
2003	050	53.65	−164.64	19	6.6	14.3
2003	076	51.27	177.98	33	7.0	3.4
2003	166	51.55	176.92	20	6.5	2.7
2003	167	55.49	160	175	6.9	352.8
2003	174	51.44	176.78	20	6.9	2.6
2003	265	19.78	−70.67	10	6.4	91.8
2003	270	50.04	87.81	16	7.3	313.3
2003	301	43.84	147.75	65	5.8	343.7
2003	339	55.54	165.78	10	6.6	356.2
2004	120	10.81	−86	10	6.2	88.9
2004	162	55.68	160	189	6.8	352.8
2004	180	54.8	−134.25	20	6.8	30.2
2004	283	11.42	−86.67	35	6.9	88.9
2004	320	4.7	−77.51	15	7.2	100.5
2004	325	13.38	−90.06	41	6.3	85.2
2004	333	43.01	145.12	39	7.0	342.6
2004	353	48.46	156.31	11	6.2	351.5
2005	018	42.95	144.87	42	6.2	343.2
2005	080	−24.98	−63.47	579	6.8	131.0
2005	141	−3.29	−80.99	40	6.3	103.3
2005	164	−19.99	−69.2	116	7.8	123.0
2005	165	51.23	179.41	51	6.8	6.7
2005	165	51.23	179.41	51	6.8	4.8
2005	166	41.3	−125.97	10	7.2	44.4
2005	168	40.77	−126.57	10	6.6	41.9
2005	264	43.89	146.15	103	6.0	342.9
2005	269	−5.68	−76.4	115	7.5	108.9
2005	288	46.82	154.11	43	6.1	351.1
2005	339	−6.22	29.83	22	6.8	223.5
2006	023	−6.86	−77.79	14	6.2	98.7
2006	053	−21.32	33.58	11	7.0	221.7
2006	110	60.95	167.09	22	7.6	359.0
2006	130	52.51	−169.26	18	6.4	13.9
2006	165	51.75	177.08	14	6.5	4.8
2006	173	45.42	149.34	95	6.0	346.3
2006	189	51.21	−179.31	22	6.6	7.3
2006	236	51.15	157.52	43	6.5	353.4
2006	265	−26.87	−63.15	598	6.0	131.7
2006	273	46.35	153.17	11	6.6	349.1
2006	274	46.47	153.24	19	6.5	349.9
2006	293	−13.46	−76.68	23	6.7	117.7
2006	317	−26.04	−63.22	552	6.8	135.4
2007	013	46.24	154.52	10	8.1	347.6
2007	055	−7.01	−80.49	23	6.3	110.7
2007	068	43.22	133.53	441	6.0	334.2
2007	119	52.01	−179.97	117	6.2	7.5
2007	150	52.14	157.29	116	6.4	352.1
2007	196	52.48	−168.05	10	6.1	13.4
2007	210	53.64	169.7	26	5.9	0.2
2007	214	51.31	−179.97	21	6.7	6.7
2007	227	−13.39	−76.6	39	8.0	117.5
2007	230	−13.81	−76.29	30	6.0	118.3
2007	246	45.84	150.06	94	6.2	347.1
2007	253	2.98	−77.97	31	6.8	104.5
2007	318	−22.25	−69.89	40	7.7	124.6
2007	320	−2.31	−77.84	123	6.8	109.7
2007	353	51.36	−179.52	29	7.2	7.9
2007	355	51.36	−178.98	30	6.3	8.2
2007	360	52.58	−168.2	35	6.4	14.5
2008	035	−20.17	−70.04	44	6.3	122.5
2008	063	46.41	153.18	10	6.5	349.8
2008	106	51.85	−179.36	10	6.5	5.0
2008	107	51.88	−179.16	13	6.6	8.0
2008	141	51.16	178.76	27	6.3	357.1
2008	179	11.01	91.82	17	6.6	276.9
2008	180	10.85	91.71	15	6.1	276.7
2008	187	53.88	152.89	633	7.7	351.0
2008	239	−7.64	−74.38	154	6.4	110.8

Table 1. (continued)

Year	Julian Day	Latitude (°)	Longitude (°)	Depth (km)	M_w	BAZ (°)
2008	286	−20.12	−64.97	353	6.2	129.9
2008	329	54.2	154.32	492	7.3	351.9
2009	015	36.86	155.15	36	7.4	351.3
2009	033	−13.58	−76.56	21	6.0	113.8
2009	040	−6.57	−81.15	15	5.9	109.9
2009	046	−5.85	−80.89	21	6.0	107.4
2009	**089**	**56.55**	**−152.74**	**21**	**6.0**	**18.0**
2009	**097**	**46.05**	**151.55**	**31**	**6.9**	**348.7**
2009	103	33.17	96.55	17	6.9	305.1
2009	**107**	**−19.58**	**−70.48**	**25**	**6.1**	**120.2**
2009	**108**	**46.01**	**151.43**	**35**	**6.6**	**349.9**
2009	111	50.83	155.01	152	6.2	351.8
2009	**123**	**14.57**	**−91.17**	**124**	**6.3**	**83.4**
2009	187	50.44	176.99	22	6.1	2.8
2009	**222**	**14.10**	**92.89**	**5**	**7.5**	**289.3**
2009	**264**	**27.33**	**91.44**	**14**	**6.1**	**295.8**
2009	**267**	**18.82**	**−107.35**	**10**	**6.4**	**72.6**
2009	**286**	**52.75**	**−167.00**	**24**	**6.4**	**15.9**
2009	**317**	**−19.39**	**−70.32**	**27**	**6.5**	**127.1**
2009	**318**	**−22.97**	**−66.64**	**220**	**6.2**	**132.0**
2009	**321**	**52.13**	**−131.40**	**3**	**6.6**	**35.3**
2009	**344**	**53.42**	**152.76**	**656**	**6.3**	**352.1**
2009	**358**	**42.23**	**134.70**	**411**	**6.3**	**331.4**
2010	**010**	**40.65**	**−124.69**	**29**	**6.5**	**47.0**
2010	012	18.45	−72.55	13	7.0	93.3
2010	037	46.84	152.73	30	6.0	348.1
2010	049	42.59	130.7	578	6.9	323.7
2010	089	13.67	92.83	34	6.6	279.6
2010	103	33.17	96.55	17	6.9	304.7
2010	126	−18.06	−70.55	37	6.2	123.1
2010	144	−8.08	−71.56	581	6.4	118.4
2010	169	44.45	148.69	25	6.2	336.0
2010	181	16.4	−97.78	20	6.3	80.3
2010	199	52.88	−169.71	25	6.7	13.5
2010	216	51.42	−178.65	27	6.4	8.4
2010	224	−1.27	−77.31	207	7.1	109.4
2010	246	51.45	−175.87	24	6.5	0.5
2010	281	51.37	−175.36	19	6.4	10.4
2010	357	53.13	171.16	18	6.4	1.9
2011	001	−26.79	−63.09	577	7.0	135.9
2011	097	17.21	−94.34	166	6.7	81.2
2011	171	−21.7	−68.23	128	6.5	129.2
2011	175	52.07	−171.84	52	7.3	9.5
2011	245	52.17	−171.71	32	6.9	12.4
2011	279	−24.18	−64.22	15	5.9	132.0
2011	301	−14.44	−75.97	24	7.0	118.9
2011	326	−15.36	−65.09	550	6.6	128.1
2011	345	17.84	−99.96	54	6.5	74.3
2012	057	51.71	95.99	12	6.7	318.8
2012	065	−28.25	−63.29	554	6.1	132.5
2012	080	16.5	−98.22	20	7.5	81.2
2012	102	18.23	−102.69	20	6.7	76.8

[a]Bold events are recorded on an OBS.

The waveforms were band pass filtered between 0.03 Hz and 0.08 Hz with a four-pole Butterworth filter. Microseismic noise determined the high-frequency end of this filter. Since the OBSs rested atop sediment, the instruments were subject to long-period noise, which determined the low-frequency end of the filter. Furthermore, we ignore waveforms with signal-to-noise ratios less than 5, consistent with what *Wüstefeld and Bokelmann* [2007] found as the lowest limit for automatic detection of null measurements. The analysis window included 20–40 s of preevent noise, with the end of the window typically limited by predicted arrivals of later seismic phases.

Individual measurements before stacking varied in quality from station to station (Figure 4). Typically on the OBSs, *SKS* arrivals were clear on the filtered waveforms, but relatively high noise levels affected some

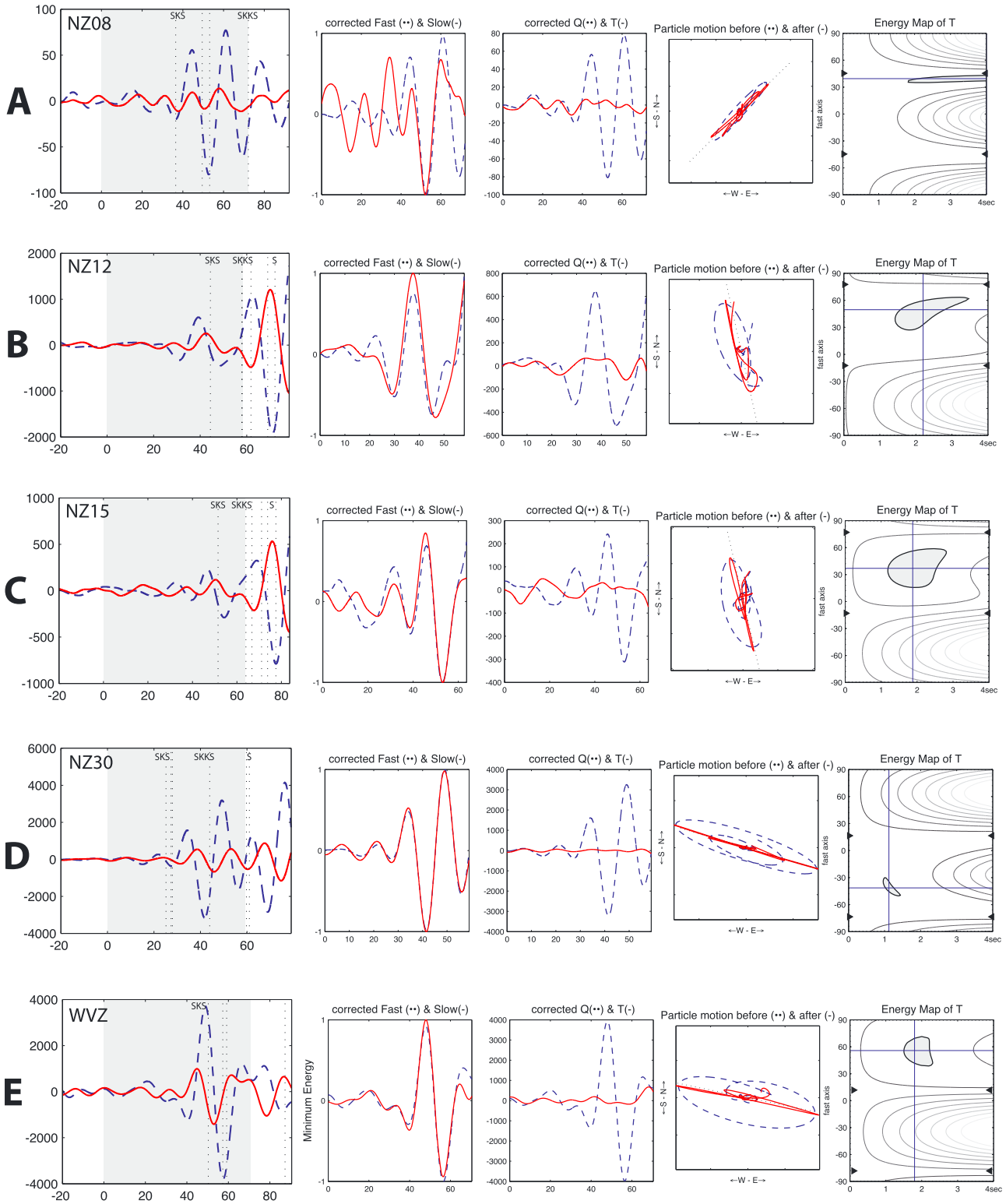

Figure 4. Examples of splitting measurements showing (first column) the filtered waveforms with analysis windows depicted by grey shading, (second column) the waveforms corrected first for delay time and then for (third column) both delay time and orientation of the fast quasi-shear wave, the particle motion before (dashed blue line) and after (solid red line) the (fourth column) effects due to splitting are removed, and (fifth column) resulting contours of transverse energy. The filled grey contour represents the 95% confidence region of δt-φ space. The dashed blue lines in the seismogram in the left column are the radial components and the solid red the transverse. (a) Event 2010010 recorded at NZ08. (b) Event 2009097 recorded at NZ12. (c) Event 2009108 recorded at NZ15. (d) Event 2009222 recorded at NZ30. (e) Event 2004320 recorded on WVZ. Event details are in Table 1.

measurements (Figures 4b and 4c). This is evident by the absence of linearized particle motions as well as the large 95% confidence intervals calculated for splitting measurements at such stations. Some measurements on OBSs, however, were comparably precise to those made on land stations. These waveforms (compare Figures 4d and 4e) have high signal-to-noise ratios, linear particle motions, and tightly constrained splitting parameters.

Some stations yielded null measurements (Figure 4a). In such cases, an error ellipse contour elongated in the δt direction for φ aligned parallel or perpendicular to the back azimuth and low energy on the raw transverse component suggests either that there may be no anisotropy underlying the station or alternatively that the azimuth of the fast orientation is parallel or perpendicular to the back azimuth of the event but with δt poorly constrained. This is evident in the individual energy contours from station NZ09 seen in the left column of Figure 5. Individual contours in Figure 5a–5d exhibit one of the shortcomings of *Silver and Chan*'s method, discussed in the previous section. For each *SKS* phase, noise and/or small birefringence at this station forces the predicted orientation of the fast quasi-shear wave along the back azimuth of the earthquake, with the predicted delay time approaching the maximum allowed time in the analysis (in this case, 4.0 s). When the contoured energy distributions are stacked, however, the resulting sum shows that these measurements are consistent with one another and yield precise estimates of φ and δt (Figure 5e). Likewise, the individual contours for earthquakes with different back azimuths in Figures 5f–5h from station NZ13 show clear anisotropy; none reveals a tightly constrained orientation or delay time, but the resulting stack (Figure 5j) does constrain φ and δt.

We also analyzed the individual seismograms for some measurements both before and after correcting for anisotropy with the average φ and δt calculated from the stacked measurements at that station (Figure 6). The averages for φ and δt obtained from the stack (Figure 7 and Table 2) are consistent with what the individual measurements allow, suggesting that a one-layer model is sufficient to explain the data.

Stations NZ08, NZ22, and NZ23 yielded null measurements, though these are constrained by a single event with a back azimuth parallel to the predicted orientation of the fast quasi-shear wave. Some stations, including stations NZ06, NZ07, NZ14, NZ19, and NZ21, yielded no useable measurements due to high levels of noise in the waveforms. We should note that in analysis of DCZ, the north and east components of the instrument were switched, consistent with phase arrivals in the seismic record.

In central portions of the South Island and within close proximity to the Southern Alps (a zone roughly 100–200 km wide), the orientations of fast polarization directions are nearly parallel to relative plate motion (roughly 240°, as averaged over the past 20 Myr in a reference frame fixed to the Australian plate [*Cande and Stock*, 2004]). Delay times are between about 1.5–2.0 s (Figure 7). In the extreme north of the island, including the Marlborough Fault Zone, orientations of the fast quasi-shear wave remain nearly parallel to relative plate motion with delay times again upward of 2.0 s; however, the mantle under some of these stations may have interacted with, or even include, the subducting Pacific plate. In the southern portion of the island, especially at stations >100 km southeast of the Alpine fault, fast orientations are more oblique to relative plate motion. In south central portions of the South Island, including DCZ, EAZ, MLZ, PYZ, and WHZ (Figure 7), fast orientations are rotated approximately 40° counterclockwise from plate motion. This obliquity increases to nearly 60–70° at stations near the southeastern coast of the South Island (ODZ, OPZ, SYZ, and TUZ). Delay times observed at these stations remain around 1.0 s. On both Stewart Island and the Chatham Islands, very little splitting is observed; delay times are only 0.4 s. The fast orientation seen on Stewart Island is consistent with the obliquity seen elsewhere on the southern portions of the South Island. Individual measurements made on the Chatham Islands yielded null or near-null results, consistent with previous observations [*Klosko et al*., 1999]. Stacking these results gives an observed fast orientation nearly E-W, but the calculated delay time is negligibly small (0.4 s), and the number of events originating in the Aleutians and Kuril Trench may bias this result.

Within about 100 km offshore of the west coast, most shear wave splitting measurements yielded fast axis orientations parallel (stations NZ11 and NZ15) or approximately parallel (station NZ12) to the orientation of relative plate motion. As seen on land for those stations within 100 km of the Alpine fault, delay times observed at the OBSs range from just over 1 s up to 2.4 ± 0.7 s. At stations deployed around 200 km offshore the west coast (i.e., stations NZ13, NZ16, and NZ18), delay times remain relatively large in magnitude around 1.5 s. Unlike those OBSs immediately off the coast, these stations yielded fast orientations rotated between 40° and

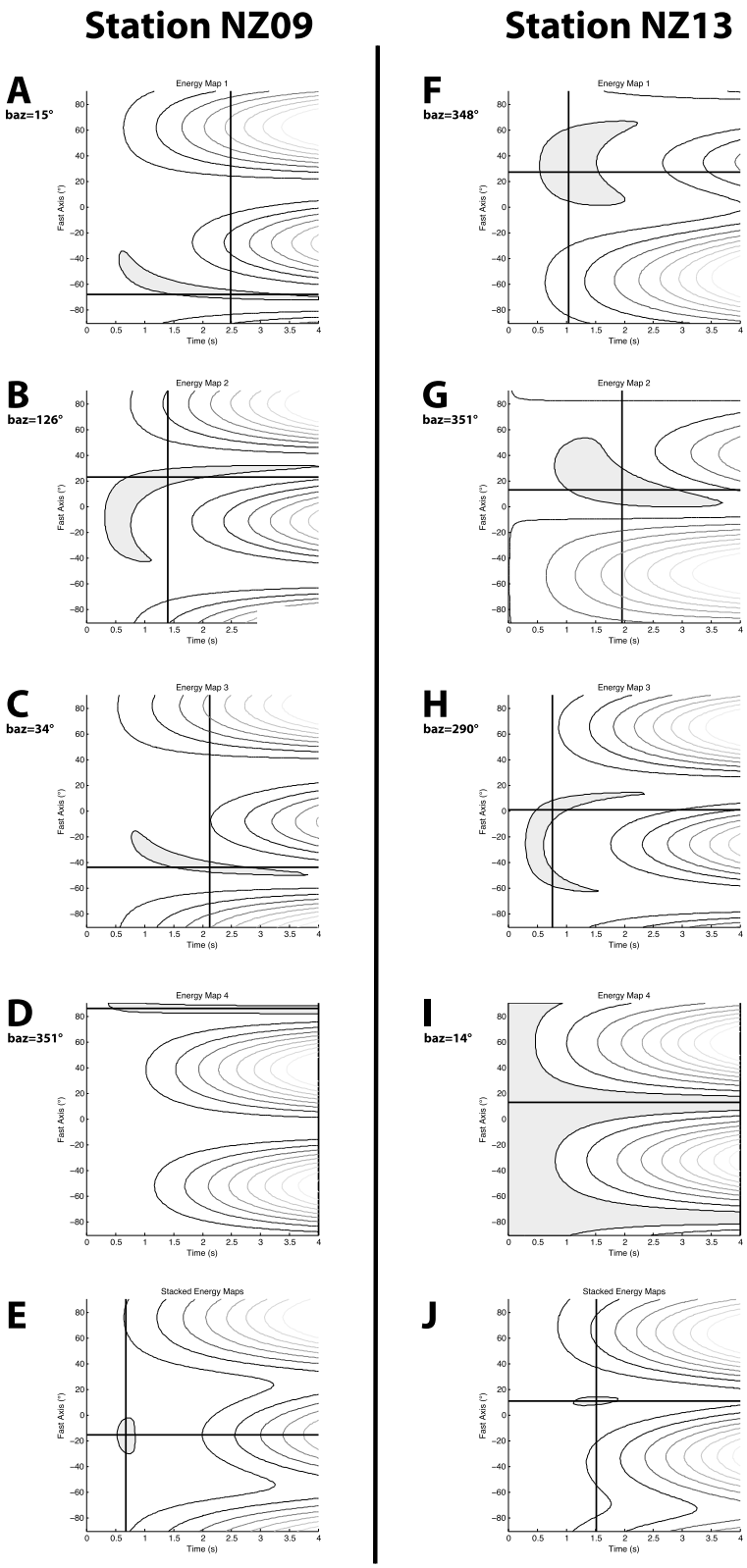

Figure 5. (a–d) Individual energy contours from individual splitting measurements made at NZ09. (e) Resulting stack of contours shown in Figures 5a–5d. (f–i) Individual energy contours from NZ13. (j) Stack of individual energy contours from NZ13 shown in Figures 5f–5i. The grey contour is the 95% confidence interval. The intersection of the black lines defines the best fitting splitting parameters.

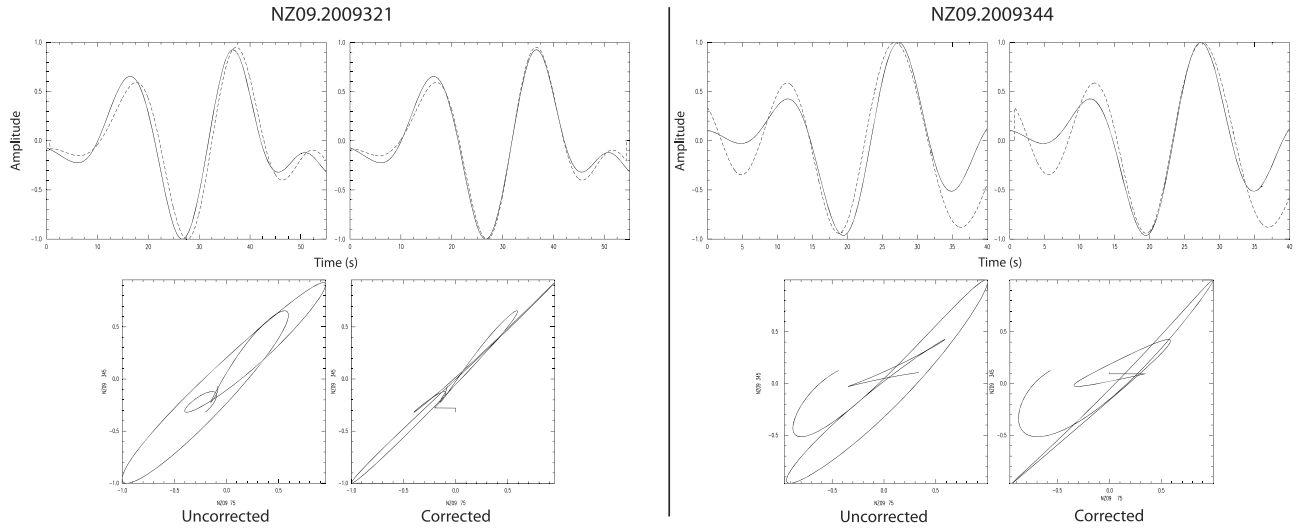

Figure 6. (top) Superposition of the fast (φ direction) and slow ($\varphi + 90°$) components and (bottom) the uncorrected and corrected particle motions for (left) event 2009321 and (right) event 2009344 at NZ09.

50° counterclockwise from relative plate motion. Beyond 300 km from the west coast, we observed a region with little to no resolvable anisotropy. The stations with minor resolvable anisotropy in this region (stations NZ05 and NZ09) show fast axes rotated almost 90° to that of relative plate motion with delay times around 0.5 s. The only useable measurement at station NZ08 yielded a null result.

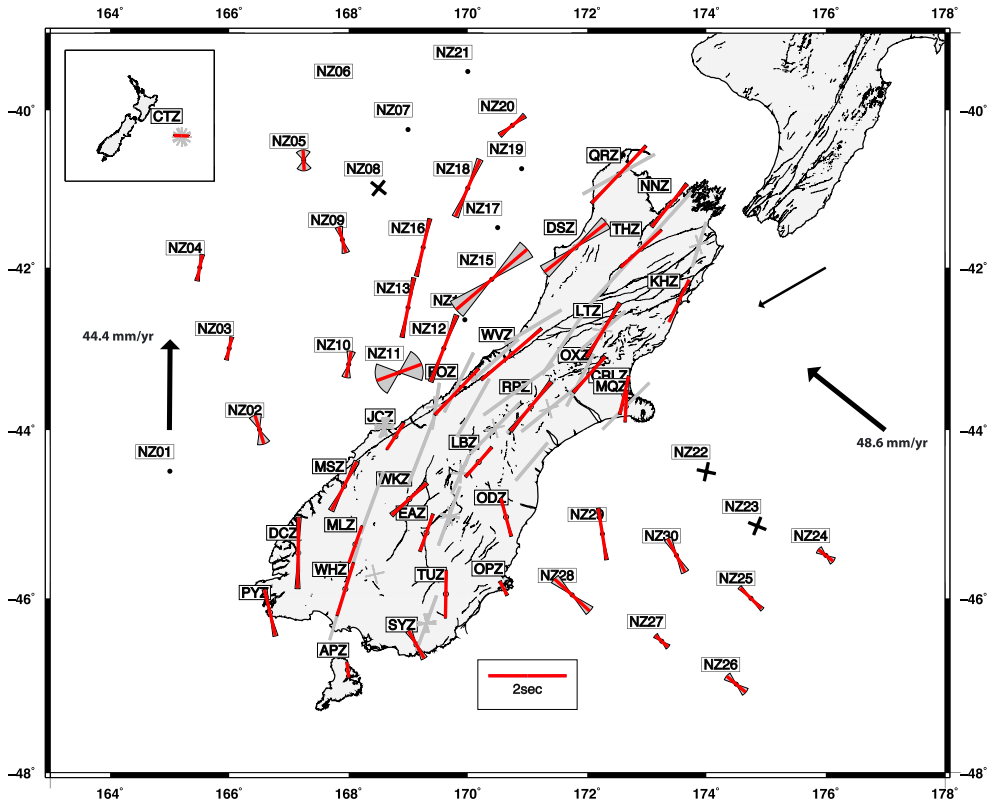

Figure 7. Summary of *SKS* splitting measurements made in this study. Red bars indicate orientations of the polarizations of the faster quasi-shear wave, and black crosses indicate null measurements. Grey wedges define uncertainties in measured orientations of fast quasi-shear waves (uncertainties are also found in Table 2). Black dots mark stations at which no useable measurements were made. Thick black arrows show current absolute plate motion of the Pacific and Australian plates in a hotspot reference frame with no net rotation [*Gripp and Gordon*, 2002]. The thin black arrow shows plate motion relative to the Australian plate averaged over 20 Ma. *SKS* splitting measurements from *Klosko et al.* [1999] and *Duclos et al.* [2005] plotted in light grey.

Table 2. Summary of Splitting Results by Station, Utilizing the *Wolfe and Silver* [1998] Stacking Method

Station	δt (s)	Error δt (s)	φ (°)	Error φ (°)	No. of Events
NZ02	0.8	0.5	−17.2	24.3	4
NZ03	0.6	0.2	13.1	10.1	8
NZ04	0.7	0.2	11.1	10.1	6
NZ05	0.5	0.5	−3.0	40.5	3
NZ06	-	-	-	-	-
NZ07	-	-	-	-	-
NZ08	null	null	39.0/129.0	4.0	1
NZ09	0.7	0.2	−15.2	16.2	4
NZ10[a]	0.7	0.3	11.1	18.2	5
NZ11[a]	1.2	1.3	69.8	40.5	3
NZ12[a]	1.8	0.8	21.2	4.0	2
NZ13[a]	1.5	0.4	11.1	4.0	4
NZ14	-	-	-	-	-
NZ15[a]	2.4	0.7	49.6	12.1	2
NZ16[a]	1.5	0.7	13.1	4.0	4
NZ18	1.6	0.6	23.3	6.1	3
NZ19	-	-	-	-	-
NZ20	0.8	0.2	51.6	10.1	4
NZ21	-	-	-	-	-
NZ22	null	null	−78.0/12.0	4.0	1
NZ23	null	null	−68.0/22.0	12.0	1
NZ24	0.5	0.3	−51.6	24.3	4
NZ25	0.8	0.1	−45.5	8.1	8
NZ26	0.6	0.3	−49.6	20.2	5
NZ27	0.4	0.2	−47.5	18.2	4
NZ28	1.2	0.4	−47.5	12.1	3
NZ29	1.3	0.2	−9.1	4.0	5
NZ30	1.0	0.1	−27.3	12.1	5
APZ	0.4	0.1	−7.1	8.1	35
CRLZ[a]	1.0	0.2	13.1	4.0	21
CTZ	0.4	0.1	−88.0	4.0	23
DCZ	1.8	0.2	1.0	4.0	21
DSZ[a]	2.0	0.4	51.6	10.1	6
EAZ[a]	1.0	0.2	19.2	4.0	29
FOZ[a]	1.6	0.2	43.5	2.0	25
JCZ[a]	0.8	0.1	33.4	2.0	22
KHZ	1.2	0.1	25.3	4.0	28
LBZ[a]	1.0	0.1	41.5	4.0	35
LTZ	1.6	0.2	31.4	4.0	21
MLZ	1.0	0.1	19.2	2.0	24
MQZ[a]	0.8	0.1	3.0	4.0	10
MSZ	1.4	0.2	27.3	6.1	11
NNZ	1.4	0.2	39.4	4.0	23
ODZ[a]	1.0	0.2	−15.2	4.0	32
OPZ	0.4	0.1	−27.3	12.1	13
OXZ[a]	1.2	0.1	41.5	4.0	14
PYZ	1.2	0.2	−13.1	6.1	13
QRZ	2.0	0.2	43.5	2.0	21
RPZ[a]	1.6	0.2	39.4	4.0	30
SYZ	0.8	0.2	−29.3	12.1	13
THZ	1.4	0.2	47.5	2.0	23
TUZ	1.2	0.2	1.0	2.0	23
WHZ	1.4	0.2	17.2	2.0	19
WKZ[a]	1.2	0.2	47.5	6.1	27
WVZ[a]	2.0	0.1	49.6	2.0	25

[a]Stations that lie in the central portion of the South Island within 200 km of the center of the shear zone. We used only these stations in the error calculations found in Table 3 and in Figures 8–10.

The three stations deployed off the continental shelf and on oceanic lithosphere (NZ02–NZ04) also exhibit a very different sense of anisotropy, with fast axis orientations trending almost due north and delay times around 0.7 s. Offshore of the east coast, fast directions are consistently nearly perpendicular to relative plate motion between the Pacific and Australian plates. Delay times calculated at these stations also remained consistent across the region, ranging between about 0.5 and 1.0 s.

5. Relationship of Anisotropy to Mantle Deformation

The shear wave splitting results clearly indicate a finite width over which the observed anisotropy could be due to simple shear between two plates. Off the east coast, the orientations of the fast quasi-shear waves are nearly aligned with current absolute plate motion of the Pacific plate calculated from HS3-NUVEL1A with no net rotation (Figure 7) [*Gripp and Gordon*, 2002]. Likewise, the fast orientations measured at the OBSs deployed off the west coast on oceanic lithosphere appear oriented parallel to absolute plate motion of the Australian plate. Offshore the west coast at stations deployed on the continental shelf, there is a decrease in the magnitude of the delay times as well as increase in the counterclockwise rotation of the fast axis orientations with increasing distance from the South Island. Furthermore, at distances 300 km and greater from the west coast, there appears to be little observable splitting. Thus, areas of anisotropy generated by different tectonic processes appear to bookend the region apparently affected by simple shear associated with relative plate motion. The symmetry of the anisotropy on either side of the Alpine fault in central regions of the South Island is also interesting, since this implies that strain is relatively uniform on either side.

The general trend of decreasing delay time observed off the west coast from the northeast toward the southwest (i.e., NZ11, NZ12, NZ14, and NZ15) is mimicked on land, with delay times of 2.0 s observed in the extreme northwest of the island (QRZ) versus delay times of closer to 1.0 s observed in the southwest (i.e., JCZ). This feature may result from the more than 800 km of motion known to have occurred between the Pacific and Australian plates over the past 45 Ma, with northwestern regions seeing more relative displacement compared to those farther south.

To discriminate between the two currently proposed mechanisms of deformation shown in Figure 2, we compare these shear wave splitting results to predictions made from both a thin viscous sheet model (mimicking distributed lithospheric deformation shown in Figure 2a) and a model in which strain within the lithosphere is localized and anisotropy is produced by distributed strain in the asthenosphere (Figure 2b).

5.1. Lithospheric Deformation: Thin Viscous Sheet Model

For a thin viscous sheet, we follow *England et al*. [1985]. In such a model, horizontal components of velocity are assumed to be independent of depth, a reasonable assumption when the tractions on the base of the sheet are small compared to stresses within the sheet. They assume that deformation of the sheet obeys a constitutive law of the following form: $\dot{\varepsilon} \sim \tau^n$, where $\dot{\varepsilon}$ is strain rate, τ is deviatoric stress, and n is the exponent of the non-Newtonian rheological model. From *England et al*. [1985], the approximate velocity field as a function of distance from the deforming boundary decays as

$$\bar{u}(x,y) \equiv U_0 \sin\left({}^{2\pi x}/_{\lambda}\right) e^{-\left({}^{4\sqrt{n}\pi y}/_{\lambda}\right)} \tag{1}$$

where U_0 is the component of velocity parallel to the deforming boundary (18 mm/yr in this study or half the total observed relative plate motion [*Beavan et al*., 1999]), x is the parallel distance along the boundary, λ is the wavelength of deformation (twice the length of a deforming boundary of finite length), and y is the perpendicular distance from the boundary. In this study, we assume that $n = 3$. Equation (1) is most accurate near the maxima and minima of the horizontal velocity (i.e., when x is close to $\lambda/4$) [*England et al*., 1985].

With exponentially decreasing velocity and strain, approximately 75% of relative plate motion occurs where $y < 2y_0$, where y_0 is the e-folding width (the value of y where the velocity decays to $1/e$ of its original value) of equation (1):

$$y_0 = {}^{\lambda}/(4\sqrt{n}\pi) \tag{2}$$

We note that *England et al*. [1985] formulated equation (1) for a semiinfinite region in the x-y plane for $y > 0$ and therefore for only one side of a deforming boundary. As we are concerned with predicted motion on both sides of a deforming boundary, we assume symmetry in the velocity field. Thus, we define the total width of deformation due to the deforming boundary as $4y_0$, again within which approximately 75% of the relative displacement of the plates has been accommodated. For a fixed exponent of the non-Newtonian rheological model n, equation (2) indicates that for a given value of y_0, there is a corresponding value of λ, the along-strike wavelength of deformation. Since λ is twice the length of the deforming boundary, we can also predict the length of the deforming boundary from y_0 or from an inferred width of deformation.

5.2. Asthenospheric Deformation

For the case of shear in the asthenosphere, strain rate decreases with depth in a fan-like shape beneath the lithosphere-asthenosphere boundary (Figure 2b). Where the strain rate becomes sufficiently small, dislocation creep is no longer the dominant mechanism of deformation, and lattice-preferred orientation does not develop. Assuming that strain from absolute plate motion is negligible compared to the strain generated in the fan-like shape beneath the fault, and assuming a constant viscosity in the asthenosphere, we adopt a toroidal velocity field of the following form, in which the only nonzero component is that parallel to what is assumed to be a fixed boundary [*Savage et al*., 2004]:

$$u_y \equiv U_0\left(1 - {}^{2\theta}\!/_{\pi}\right), \tag{3}$$

where U_0 again is the component of velocity parallel to a strike-slip boundary ($U_0 = 18$ mm/yr), $\theta = \arcsin(z/r)$, $r = (y^2 + z^2)\text{^}(1/2)$, $z =$ depth, and $y =$ perpendicular distance from the fault. The only nonzero component of the strain rate tensor for this velocity field is [*Savage et al*., 2004]

$$\dot{\varepsilon} = \pm {}^{U_0}\!/_{\pi r}. \tag{4}$$

To determine whether or not a transition from dislocation to diffusion creep is feasible at a specified depth given the strain rates predicted from equation (4), we use the synthesis of laboratory experiments given by *Hirth and Kohlstedt* [2003]. The strain rate of minerals in a steady state is

$$\dot{\varepsilon} = A\sigma^m d^{-p} C_{OH}{}^r \exp[-(E^* + PV^*)/(RT)], \tag{5}$$

where $\dot{\varepsilon}$ is the strain rate, A is a preexponential factor, σ is shear stress, m is the stress exponent, p is the grain size exponent, d is grain size, C_{OH} is water content, r is the water content exponent, E^* is the activation energy, P is pressure, V^* is the activation volume, R is the gas constant, and T is temperature in Kelvin. In a dislocation creep regime at constant OH concentrations (1000 H/10^6Si), $A = 90$ (for stress in megapascal, C_{OH} in H/10^6Si, and grain size in micrometer), $m = 3.5 \pm 0.3$, $p = 0$, $r = 1.2$, $E^* = 480 \pm 40$ kJ/mol, and $V^* = 11 \times 10 - {}^6$ m^3/mol. In a diffusion creep regime at constant OH concentrations (again, 1000 H/10^6Si), $A = 1.0 \times 10^6$ (again, for stress in megapascal, C_{OH} in H/10^6Si, and grain size in micrometer), $m = 1$, $p = 3$, $r = 1$, $E^* = 335 \pm 75$ kJ/mol, and $V^* = 4.0 \times 10^{-6}$ m^3/mol. We calculate pressure by assuming it is 1 GPa at the base of the crust with a pressure gradient of 30 MPa/km below this. At the lithosphere-asthenosphere boundary, we assume a temperature of 1573 K, with an adiabatic gradient of 0.5 K/km deeper into the asthenosphere. The unknowns for which we must solve in equation (5) are shear stress and grain size.

To solve for these unknown parameters, we first predict strain rate as a function of depth using equation (4). Given this strain rate, the temperature and pressure at a specified depth, and the parameters for dislocation creep listed above, we next predict the shear stress required to yield the same strain rate given by equation (4) using the flow law given in equation (5) for dislocation creep (i.e., when $p = 0$). Then, using this predicted shear stress, we determine the corresponding grain size that gives the same strain rate using equation (5) in its diffusion creep form (i.e., when $p = 3$). For instance, if the transition between dislocation creep and diffusion creep occurred 100 km into the asthenosphere ($z_0 = 100$ km, where z_0 is the distance from the lithosphere-asthenosphere boundary to the depth of the transition between dislocation and diffusion creep directly under the deforming boundary), this model would require a shear stress of ~0.2 MPa and a grain size of ~6 mm. For a transition at 150 km into the asthenosphere ($z_0 = 150$ km), a shear stress of ~0.2 MPa and a grain size of ~7 mm is required, and a transition at 200 km below the lithosphere-asthenosphere boundary also requires a shear stress of ~0.2 MPa, but a grain size of ~8 mm. Although strain rate decreases with depth, stresses increase to compensate for the influence of activation volume in the factor that includes it in equation (5).

5.3. Predicted Patterns of Anisotropy

To generate a predicted pattern of anisotropy from the models discussed above, we follow relationships outlined in *Ribe* [1992] and *Kaminski and Ribe* [2002]. We first convert the predicted strain rates from each model into strain following *McKenzie and Jackson* [1983], who showed that in the case of simple shear, strain can be calculated by simply multiplying strain rate by the time over which the strain has accumulated. Modeling by *Savage et al*. [2007] suggests that the widespread anisotropy observed on the South Island is primarily a result of strike-slip deformation, with little effect from convergence. Thus, we ignore the

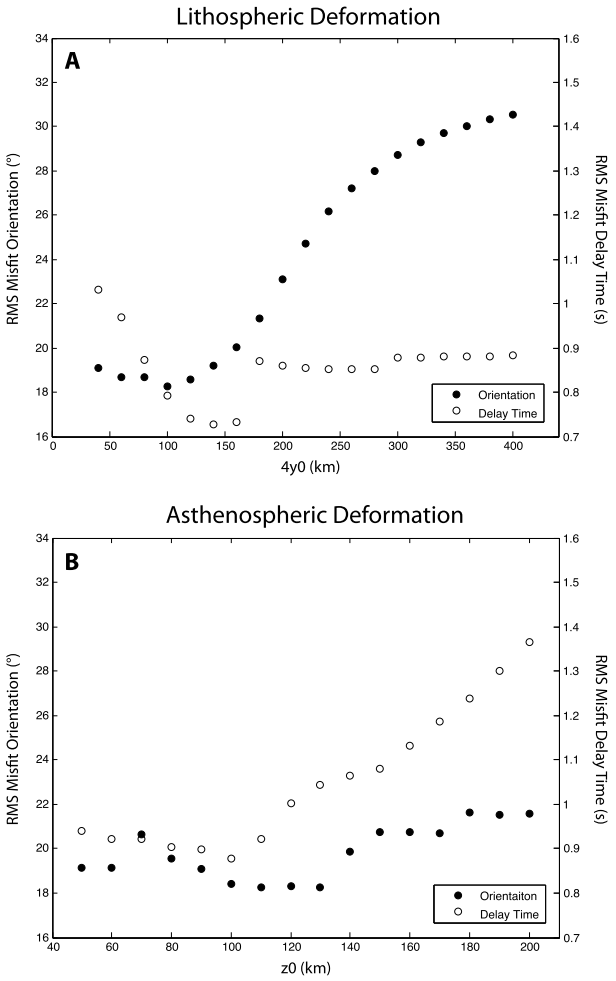

Figure 8. Calculated RMS misfit in predicted orientation of the fast quasi-shear wave relative to motion between the Australian and Pacific Plates and predicted delay time for (a) a model of lithospheric deformation and (b) a model for asthenospheric deformation.

compressional component of motion between the Pacific and Australian plates and assume all the strain accumulation is due to finite simple shear parallel to relative motion between the Pacific and Australian plates. Following *Sutherland* [1999], about 850 km of strike-slip motion has occurred between the Pacific and Australian plates. We assume the time over which this strain accumulated is equal to the time required to displace 850 km of the fault at the present rate of 36 mm/yr, yielding about 24 Ma and maximum strain rates on the order of 10^{-14} to 10^{-15} s^{-1}. Although the predicted strain in the asthenosphere includes a plunge, we examine only the horizontal projection of that strain.

Numerical models of polycrystalline flow [*Kaminski and Ribe*, 2002] suggest that at temperatures appropriate for the asthenosphere, lattice-preferred orientation develops in three stages. For strains less than 0.2, the LPO follows the evolution of the finite strain ellipsoid. For strains between 0.2 and 1.2, however, the LPO evolves faster than the finite strain ellipsoid, which *Kaminski and Ribe* [2002] parameterize using a model for dynamic recrystallization. We estimate orientations for such strains from the mean orientation of the olivine *a* axis in simple shear given in *Kaminski and Ribe* [2002]. For strains larger than 1.2, olivine *a* axes reach a steady state orientation within the shear plane parallel to the shear direction. We note that *Zhang and Karato's* [1995] experiments, used by *Kaminski and Ribe* [2002], were conducted at high temperatures (1300°C), and although others have shown similar relationships at slightly lower temperatures of 1200°C [*Bystricky et al.*, 2000], tests of *Kaminski and Ribe's* [2002] parameterization have not been made for lithospheric temperatures.

Using laboratory-based flow laws for single crystals, *Ribe* [1992] calculated percent anisotropy as a function of natural strain for olivine aggregates. We used *Ribe's* [1992] relationship for an aggregate composed of 70%

Table 3. Calculated RMS Misfits Between Shear Wave Spitting Measurements Made in This Study and Predictions From Both a Thin Viscous Sheet Model Representing Lithospheric Deformation (LD) and a Model Representing Asthenospheric Deformation (AD)[a]

Lithospheric Deformation	RMS Misfit φ (°)	RMS Misfit δt (s)	Asthenospheric Deformation	RMS Misfit φ (°)	RMS Misfit δt (s)
LD ($4y_0 = 40$ km)	19.1	1.0	AD ($z_0 = 50$ km)	19.1	0.9
LD ($4y_0 = 60$ km)	18.7	1.0	AD ($z_0 = 60$ km)	19.1	0.9
LD ($4y_0 = 80$ km)	18.7	0.9	AD ($z_0 = 70$ km)	20.6	0.9
LD ($4y_0 = 100$ km)	18.3	0.8	AD ($z_0 = 80$ km)	19.6	0.9
LD ($4y_0 = 120$ km)	18.6	0.7	AD ($z_0 = 90$ km)	19.1	0.9
LD ($4y_0 = 140$ km)	19.2	0.7	AD ($z_0 = 100$ km)	18.4	0.9
LD ($4y_0 = 160$ km)	20.1	0.7	AD ($z_0 = 110$ km)	18.2	0.9
LD ($4y_0 = 180$ km)	21.3	0.9	AD ($z_0 = 120$ km)	18.3	1.0
LD ($4y_0 = 200$ km)	23.1	0.9	AD ($z_0 = 130$ km)	18.2	1.0
LD ($4y_0 = 220$ km)	24.7	0.9	AD ($z_0 = 140$ km)	19.9	1.1
LD ($4y_0 = 240$ km)	26.2	0.9	AD ($z_0 = 150$ km)	20.7	1.1
LD ($4y_0 = 260$ km)	27.2	0.9	AD ($z_0 = 160$ km)	20.7	1.1
LD ($4y_0 = 280$ km)	28.0	0.9	AD ($z_0 = 170$ km)	20.7	1.2
LD ($4y_0 = 300$ km)	28.7	0.9	AD ($z_0 = 180$ km)	21.7	1.2

[a]Only those measurements in the central portion of the South Island and within 200 km of the Alpine fault were included in the error calculation (see Table 2).

olivine [*Ribe*, 1992, equation (24)] to convert our calculations of strain from each model to percent anisotropy. To predict approximate delay times from percent anisotropy, we simply multiply percent anisotropy by the layer thickness over shear wave speed, assuming that for predicted strain larger than 1.2, percent anisotropy is 10%, which is reasonable given estimates of percent anisotropy from *Pn* studies [*Bourguignon et al*., 2007; *Scherwatch et al*., 2002]; however, since the delay time between fast and slow quasi-shear waves depends on both the magnitude of anisotropy and the thickness of the anisotropic layer, we do not emphasize the absolute magnitude of the predicted delay times. Instead, we use them to address relative variations in delay time as a function of distance from the deforming boundary. In the case of a thin viscous sheet, we assume a lithospheric thickness of approximately 100 km, based on estimates of lithospheric thickness used in other studies [e.g., *Stern et al*., 2000]. By making such an assumption, we also ignore any crustal contribution to anisotropy, of which average delay times range from approximately 0.2 to 0.3 s for the South Island [*Karalliyadda and Savage*, 2013]. There is some agreement between the fast directions of local *S* phases made in *Karalliyadda and Savage* [2013] and the teleseismic *SKS* measurements made in our study, especially for southern portions of the South Island. Yet the smaller delay times calculated by *Karalliyadda and Savage* [2013] than those measured using *SKS* phases suggest that the bulk of the anisotropy must at least be deeper than the crust. For anisotropy in the asthenosphere, we assume an isotropic lithospheric thickness of 100 km, and we estimate a thickness of the underlying anisotropic zone as a function of the value chosen for z_0 as discussed in the previous section. We assume a shear wave speed of 4.5 km/s.

6. Discussion

Our shear wave splitting measurements (Figure 7) indicate that large anisotropy with the orientation of the fast quasi-shear wave nearly parallel to the direction of relative plate motion spans a zone approximately 100–200 km wide in central portions of the South Island. We estimate relevant parameters for our two models, namely, the width of deformation ($4y_0$) and corresponding length of the deforming boundary ($\lambda/2$) for the thin viscous sheet model, and shear stress (σ) and grain size (d) for a model of asthenospheric shear. Calculated RMS misfits for the orientation of the fast quasi-shear wave and delay time between our shear wave splitting measurements and these predictions for the central portion of the South Island (Figures 8a and 8b and Table 3) show that both the lithospheric deformation and asthenospheric shear models can be made to fit the data comparably well. This is not surprising since we chose model parameters so that the predicted patterns match the observed patterns.

A thin viscous sheet model with a deformation width between $4y_0 = 100$ and 140 km (Figures 9b, 9c, and 10) yields a predicted pattern of anisotropy similar to that observed (Figure 9a). These widths of deformation correspond to a deforming boundary length ($\lambda/2$) around 544–762 km, consistent with the approximate length of the boundary, as well as with ~850 km of displacement thought to have occurred between the Pacific and Australian plates over the past 45 Ma [*Sutherland*, 1999; *Cande and Stock*, 2004]. Likewise, a model of shear in the asthenosphere (Figures 9d, 9e, and 10) with a shear stress in the asthenosphere of

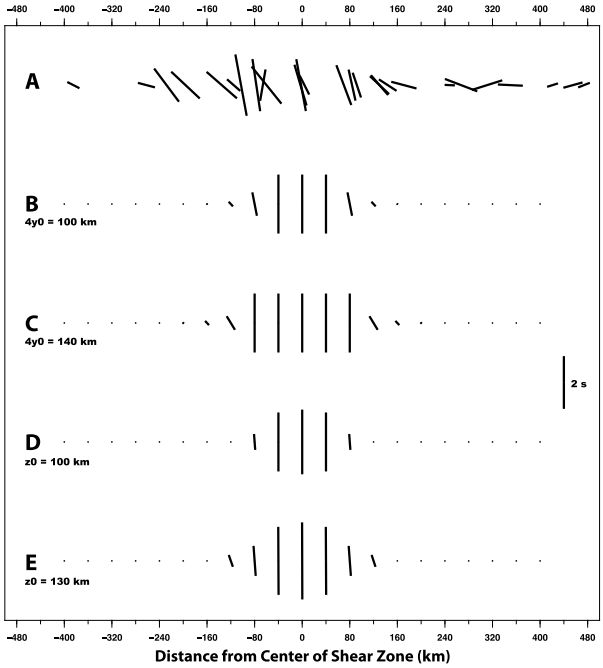

Figure 9. Comparison of observed shear wave splitting to predictions of the orientation of the fast quasi-shear wave relative to motion between the Pacific and Australian plates. Lengths correspond to delay time (δt). (a) Measurements made in this study. (b and c) Predictions from a model for lithospheric deformation with a deforming zone width of $4y_0 = 100–140$ km, respectively. (d and e) Predictions from a model for asthenospheric deformation with $\sigma = 0.21$ MPa and $d \approx 6$ mm (corresponding to $z_0 = 100$ km) and with $\sigma = 0.22$ MPa and $d \approx 7$ mm (corresponding to $z_0 = 130$ km), respectively.

approximately 0.21–0.22 MPa and with an average grain size on the order of 6 ± 1 to 7 ± 1 mm (corresponding to $z_0 = 100–130$ km) also yields a similar pattern of anisotropy to that observed.

Given the long-period filter used in making the shear wave splitting measurements, individual *SKS* waves sample a wider diameter along the geometrical raypath (i.e., larger Fresnel zone) than shorter period seismic waves. Thus, the width of the deforming zone may be narrower than the 100–200 km zone we infer. *Rümpker and Ryberg* [2000] show *SKS* phases with a dominant period of 16 s (similar to those we analyzed) arriving at a station directly above an anisotropic region sample a region 140 km wide at the surface. This sampled region becomes 180 km wide at 100 km depth and approximately 240 km wide at 200 km depth. Given the 100 km spacing of the seismic stations and the clear difference in measured anisotropy between onshore the South Island and offshore the east coast, there is no reason to think the width of the deforming zone is significantly narrower than 100–200 km wide.

Thus, the question remains; given these model parameters and other currently available data on the mantle characteristics of the South Island of New Zealand, are predictions from either model plausible? Specifically, is the lithosphere underlying the South Island and offshore thick enough to yield large delay times similar to those observed from the teleseismic shear wave splitting measurements? Are the shear stresses and grain sizes calculated here viable for producing anisotropy at asthenospheric depths?

A shear wave speed of 4.5 km/s and 10% anisotropy requires a 90 km thick anisotropic layer to yield a delay time of 2 s, similar to the largest delay times measured in this study. The crust offshore and in coastal areas of the South Island is approximately 25 km thick [*Salmon et al*., 2013]. Under the Southern Alps, the thickness increases to just over 40 km. Furthermore, recent work suggests that at temperatures below 700 ± 100°C, olivine will not flow significantly at geologic stresses [e.g., *Mei et al*., 2010] and therefore will not produce a lattice-preferred orientation. The modeling work of *Savage et al*. [2007] places the 700°C isotherm in the 40 km depth range for this region. Therefore, this would require a total lithospheric thickness of 130 km (a 40 km thick isotropic region overlying a 90 km thick anisotropic region) for the anisotropy to be completely accommodated within the lithosphere.

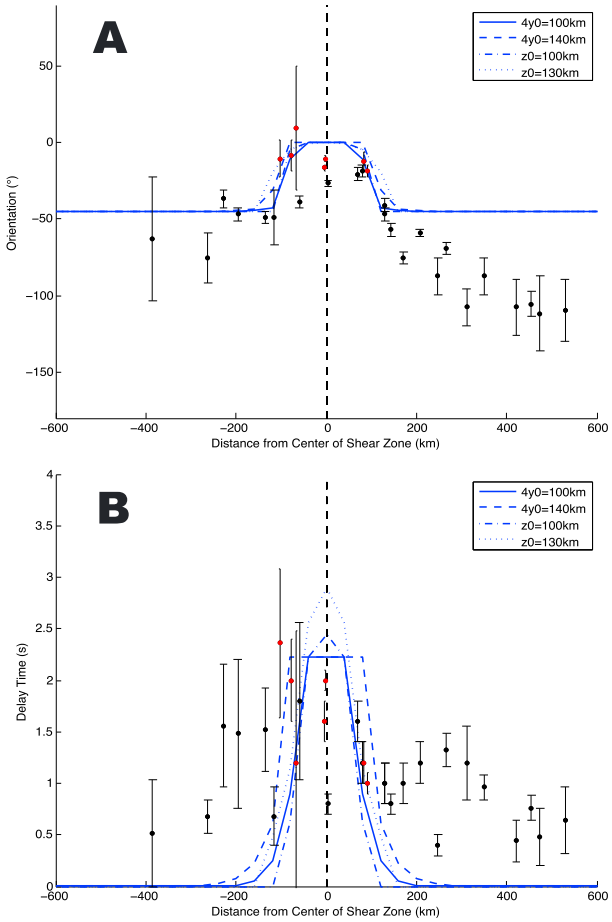

Figure 10. (a) Orientations of polarizations of fast quasi-shear waves (relative to plate motion between the Pacific and Australian plates) versus distance from the center of the shear zone. Negative and positive distances are for stations west and east of the center of the shear zone, respectively. (b) Delay time versus distance from the center of the shear zone. In both Figures 10a and 10b, red circles indicate those stations with fast direction orientations within 20° of the orientation of relative motion between the Pacific and Australian plates. These represent those measurements from the central portion of the South Island reflecting simple shear along a deforming zone.

Determining the thickness of lithosphere remains a controversial topic, though evidence from *P* wave delays suggest that the lithosphere beneath the axis of the South Island may have been thickened, perhaps by 2 times, from an original thickness of 100–120 km [*Stern et al*., 2000]. While this would imply a somewhat deeper lithosphere-asthenosphere boundary than that inferred by other studies of surrounding regions [e.g., *Rychert and Shearer*, 2009; *Fichtner et al*., 2010], *P* wave tomography using local and regional events yielded a high-velocity region to 180 km depth [*Kohler and Eberhart-Phillips*, 2002], suggesting lithosphere to this depth. Thus, we deduce that the lithosphere could host the observed anisotropy over most of the study region, especially given that larger delay times under portions of the Southern Alps might reflect thickened lithosphere.

Our model of localized lithospheric deformation with shear in the asthenosphere predicts shear stresses and grain sizes that fall within currently accepted ranges for such values. From the model strain rates and shear stresses, we calculate an effective viscosity of the asthenosphere on the order of 10^{20} Pa s, consistent with other studies [e.g., *Conrad and Behn*, 2010]. Furthermore, estimates of grain size in the asthenospheric upper mantle range from several millimeters to centimeters [*Hirth and Kohlstedt*, 2003; *Podolefsky et al*., 2004; *Becker et al*., 2008], making a grain size close to 6–7 mm (as required in this study) realistic.

More problematic is determining the grain size required for a transition from dislocation creep to diffusion creep, and therefore, the transition from a region susceptible to the formation of lattice-preferred orientation (dislocation creep) to one that is not (diffusion creep, see section 3). Some estimate this transition at about

200 km depth with a grain size around 1 cm [*Hirth and Kohlstedt*, 2003]. Later work investigated the effects of hydration on the depth of this transition as well as grain size in oceanic mantle [*Behn et al*., 2009]. *Behn et al*. [2009] found that for mantle lithosphere older than 60 Myr with an olivine water content of 1000 H/10^6Si, grain size reached a minimum of 15–20 mm at ~150 km depth or 20–30 mm at ~400 km depth, values greater than that predicted for the transition between dislocation creep and diffusion creep. Taking into account the errors associated with the parameters used in equation (5), we calculate that the transition between the creep mechanisms occurs for ranges of shear stress from 0.06 to 0.61 MPa and grain size from about 5 to 7 mm at $z_0 = 100$ km. For $z_0 = 130$ km, shear stress ranges from 0.05 to 0.67 MPa, with grain size ranging from about 5 to 8 mm. These ranges for grain size are less than the steady state grain sizes proposed by *Behn et al*. [2009]; we do not have independent constrains on how large grain size could actually be in this region.

Concerning the role of water content on the evolution of LPO, laboratory experiments show that the influence of water on predicted anisotropy is largest when B-type or C-type fabrics are produced [e.g., *Karato et al*., 2008, and references therein]. In these cases, the fast quasi-shear wave can be polarized normal, not parallel, to the orientation of shearing (horizontal flow with B-type fabric; vertical flow with C-type). In the South Island of New Zealand (at least in regions like the Southern Alps that lie outside of subduction zones), the water content is likely not high enough to induce these fabrics. Furthermore, the shear stresses in the asthenosphere calculated from our localized lithospheric deformation model are low relative to those required to promote B-type and C-type fabric. Thus, we infer that hydration of the asthenosphere does not strongly affect anisotropy beneath New Zealand.

Although this *SKS* splitting study alone cannot definitively discriminate between distributed versus localized modes of lithospheric deformation in the South Island of New Zealand, further analyses that can place a depth extent on the anisotropy will aid in this debate. A study of *Pn* travel times also utilizing the data collected during the MOANA experiment (J. A. Collins and P. H. Molnar, manuscript in preparation, 2014) shows fast *Pn* propagation for paths crossing the southeast side of the South Island to be aligned NNW-SSE, similar to that of fast quasi-shear waves. Thus, the *Pn* data suggest that some of the shear wave splitting observed at OBSs southeast of the island is within the lithosphere. Fast propagation of *Pn* for paths beneath most of the island and offshore to the northwest (in a zone 150–300 km wide) is approximately parallel to the relative motion between the Australian and Pacific plates. Hence, for that region, it is similar to the shear wave splitting measurements reported here. Splitting from local *S* phases on both the MOANA OBSs and GeoNet stations also suggest a possible lithospheric origin for the observed anisotropy (S. Karalliyadda, manuscript in preparation, 2014).

Given these new shear wave splitting measurements and the available data on the characteristics of the mantle under the South Island of New Zealand, it appears that either distributed lithospheric or asthenospheric deformation is plausible. If anisotropy is the result of distributed deformation of the mantle lithosphere, we expect a width of deformation around $4y_0 = 100$–140 km. If anisotropy is the result of localized lithospheric deformation with pervasive shear in the asthenosphere, grain sizes on the order of 6–7 mm are required at depths between 100 and 130 km below the lithosphere.

7. Conclusions

New shear wave splitting measurements made onshore and offshore the South Island of New Zealand show an approximately 100–200 km wide zone of 1.0–2.0 s delay times with orientations of the fast quasi-shear waves nearly parallel to the direction of relative motion between the Pacific and Australian plates. Regions of distinctly different patterns of anisotropy bound this zone of high anisotropy. Approximately 300 km off the west coast, little to no shear wave splitting is observed. Offshore the east coast, the anisotropy is clearly not a result of simple shear between the Pacific and Australian plates and is consistent with its being due to current absolute plate motion of the Pacific plate or frozen into the lithosphere.

We used these new shear wave splitting results to test two models of deformation to explain the observed anisotropy: (1) a thin viscous sheet model mimicking distributed deformation in the mantle lithosphere and (2) a model mimicking localized deformation in the mantle lithosphere around a fault that extends to the asthenosphere, where deformation is then accommodated in a fan-like pattern centered beneath the fault. A model of a thin viscous sheet with a width of deformation around 100–140 km could explain the observed pattern of anisotropy. Likewise, if grain size at depths of 100–130 km into the asthenosphere were ~6–7 mm,

localized lithospheric deformation with diffuse shear in the underlying asthenosphere also fits our measurements equally well. In any case, deformation in the upper mantle along this major shear zone in the South Island of New Zealand appears confined to a 100–200 km wide region.

Acknowledgments

We thank Josh Stachnik and Zhaohui Yang for their assistance in orienting the horizontal components of the OBSs and Megan Anderson for her help with the SplitLab software. We also thank the captain and crew of the R/V *Thomas G. Thompson* (cruise TN229) in 2009 and of the R/V *Roger Revelle* (cruise RR1002) in 2010. All 30 OBSs were manufactured by Scripps Institution of Oceanography and are part of the United States National Ocean Bottom Seismograph Instrumentation Pool. These data are available for download from the IRIS Data Management Center. We acknowledge the New Zealand GeoNet project and its sponsors EQC, GNS Science, and LINZ for also providing data in this study. The figures were made with the Generic Mapping Tools (GMT) software by *Wessel and Smith* [1998]. The (former) New Zealand Foundation for Research, Science and Technology, and the National Science Foundation Continental Dynamics program supported this work under grants EAR-0409564, EAR-0409609, and EAR-0409835. We also thank Editor Tom Parsons and two anonymous reviewers for their constructive comments.

References

Audoine, E., M. K. Savage, and K. R. Gledhill (2000), Seismic anisotropy from local earthquakes in the transition region from a subduction to a strike-slip plate boundary, New Zealand, *J. Geophys. Res.*, *105*(B4), 8013–8033, doi:10.1029/1999JB900444.

Babuška, V., and M. Cara (1991), *Seismic Anisotropy in the Earth*, vol. 10, Kluwer Academic Publishers, Boston, Mass.

Beavan, J., et al. (1999), Crustal deformation during 1994–1998 due to oblique continental collision in the central Southern Alps, New Zealand, and implications for seismic potential of the Alpine fault, *J. Geophys. Res.*, *104*(B11), 25,233–25,255, doi:10.1029/1999JB900198.

Becker, T. W., B. Kustowski, and G. Ekström (2008), Radial seismic anisotropy as a constraint for upper mantle rheology, *Earth Planet. Sci. Lett.*, *267*, 213–227, doi:10.1016/j.eps12007.11.038.

Behn, M. D., G. Hirth, and J. R. Elsenbeck II (2009), Implications of grain size evolution on the seismic structure of the oceanic upper mantle, *Earth Planet. Sci. Lett.*, *282*, 178–189, doi:10.1016/j.epsl.2009.03.014.

Bourguignon, S., T. A. Stern, and M. K. Savage (2007), Crust and mantle thickening beneath the southern portion of the Southern Alps, New Zealand, *Geophys. J. Int.*, *168*, 681–690, doi:10.1111/j.1365-246X.2006.03208.x.

Bystricky, M., K. Kunze, L. Burlini, and J.-P. Burg (2000), High shear strain of olivine aggregates: Rheological and seismic consequences, *Science*, *290*, 1564–1567, doi:10.1126/science.290.5496.1564.

Cande, S. C., and J. M. Stock (2004), Pacific-Antarctic-Australia motion and the formation of the Macquarie Plate, *Geophys. J. Int.*, *157*, 399–414, doi:10.1111/j.1365-246X.2004.02224.x.

Conrad, C. P., and M. D. Behn (2010), Constraints on lithosphere net rotation and asthenospheric viscosity from global mantle flow models and seismic anisotropy, *Geochem. Geophys. Geosyst.*, *11*, Q05W05, doi:10.1029/2009GC002970.

Duclos, M., M. K. Savage, A. Tommasi, and K. R. Gledhill (2005), Mantle tectonics beneath New Zealand inferred from SKS splitting and petrophysics, *Geophys. J. Int.*, *163*, 760–774, doi:10.1111/j.1365-246X.2005.02725.x.

England, P., G. Houseman, and L. Sonder (1985), Length scales for continental deformation in convergent, divergent, and strike-slip environments: Analytical and approximate solutions for a thin viscous sheet model, *J. Geophys. Res.*, *90*(B5), 3551–3557, doi:10.1029/JB090iB05p03551.

Fichtner, A., B. L. N. Kennett, H. Igel, and H.-P. Bunge (2010), Full waveform tomography for radially anisotropic structure: New insights into present and past states of the Australasian upper mantle, *Earth Planet. Sci. Lett.*, *290*, 270–280, doi:10.1016/j.epsl.2009.12.003.

Furlong, K. P. (2007), Locating the deep extent of the plate boundary along the Alpine Fault zone, New Zealand: Implications for patterns of exhumation in the Southern Alps, *Geol. Soc. Am. Spec. Pap.*, *434*, 1–14, doi:10.1130/2007.2434(01).

Gripp, A. E., and R. G. Gordon (2002), Young tracks of hotspots and current plate velocities, *Geophys. J. Int.*, *150*, 321–361, doi:10.1046/j.1365-246X.2002.01627.x.

Hirth, G., and D. Kohlstedt (2003), Rheology of the upper mantle and the mantle wedge: A view from experimentalists, inside the subduction factory, *Geophys. Monogr.*, *138*, 83–105.

Houlié, N., and T. Stern (2012), A comparison of GPS solutions for strain and SKS fast directions: Implications for modes of shear in the mantle of a plate boundary zone, *Earth Planet. Sci. Lett.*, *345–348*, 117–125, doi:10.1016/j.epsl.2012.06.029.

Kaminski, É., and N. M. Ribe (2002), Timescales for the evolution of seismic anisotropy in mantle flow, *Geochem. Geophys. Geosyst.*, *3*(8), doi:10.1029/2001GC000222.

Karalliyadda, S., and M. K. Savage (2013), Seismic anisotropy and lithospheric deformation of the plate-boundary zone in South Island, New Zealand: Inferences from local S-wave splitting, *Geophys. J. Int.*, *193*(2), 507–530, doi:10.1093/gji/ggt022.

Karato, S.-i., and P. Wu (1993), Rheology of the upper mantle: A synthesis, *Science*, *260*, 771–778, doi:10.1126/science.260.5109.771.

Karato, S.-i., H. Jung, I. Katayama, and P. Skemer (2008), Geodynamic significance of seismic anisotropy of the upper mantle: New insights from laboratory studies, *Ann. Rev. Earth Planet. Sci.*, *36*, 59–95, doi:10.1146/annurev.earth.36.031207.124120.

Klosko, E. R., F. T. Wu, H. J. Anderson, D. Eberhart-Phillips, T. V. McEvilly, E. Audoine, M. K. Savage, and K. R. Gledhill (1999), Upper mantle anisotropy in the New Zealand region, *Geophys. Res. Lett.*, *26*, 1497–1500, doi:10.1029/1999GL900273.

Kohler, M. D., and D. Eberhart-Phillips (2002), Three-dimensional lithospheric structure below the New Zealand Southern Alps, *J. Geophys. Res.*, *107*(B10), 2225, doi:10.1029/2001JB000182.

Kumazawa, M. (1969), The elastic constants of single-crystal orthopyroxene, *J. Geophys. Res.*, *74*(25), 5973–5980, doi:10.1029/JB074i025p05973.

Levin, V., D. Okaya, and J. Park (2007), Shear wave birefringence in wedge-shaped anisotropic regions, *Geophys. J. Int.*, *168*, 275–286, doi:10.1111/j.1365-246X.2006.03224.x.

Little, T. A., M. K. Savage, and B. Tikoff (2002), Relationship between crustal finite strain and seismic anisotropy in the mantle, Pacific-Australia plate boundary zone, South Island, New Zealand, *Geophys. J. Int.*, *151*, 106–116, doi:10.1046/j.1365-246X.2002.01730.x.

Long, M. D., and T. W. Becker (2010), Mantle dynamics and seismic anisotropy, *Earth Planet. Sci. Lett.*, *297*, 341–354, doi:10.1016/j.epsl.2010.06.036.

McKenzie, D., and J. Jackson (1983), The relationship between strain rates, crustal thickening, palaeomagnetism, finite strain and fault movements within a deforming zone, *Earth Planet. Sci. Lett.*, *65*, 182–202, doi:10.1016/0012-821X(83)90198-X.

Mehl, L., B. R. Hacker, G. Hirth, and P. B. Kelemen (2003), Arc-parallel flow within the mantle wedge: Evidence from the accreted Talkeetna arc, south central Alaska, *J. Geophys. Res.*, *108*(B8), 2375, doi:10.1029/2002JB002233.

Mei, S., A. M. Suzuki, D. L. Kohlstedt, N. A. Dixon, and W. B. Durham (2010), Experimental constraints on the strength of the lithospheric mantle, *J. Geophys. Res.*, *115*, B08204, doi:10.1029/2009JB006873.

Molnar, P., et al. (1999), Continuous deformation versus faulting through the continental lithosphere of New Zealand, *Science*, *286*, 516–519, doi:10.1126/science.286.5439.516.

Monteiller, V., and S. Chevrot (2010), How to make robust splitting measurements for single-station analysis and three-dimensional imaging of seismic anisotropy, *Geophys. J. Int.*, *182*, 311–328, doi:10.1111/j.1365-246X.2010.04608.x.

Moore, M., P. England, and B. Parson (2002), Relation between surface velocity field and shear wave splitting in the South Island of New Zealand, *J. Geophys. Res.*, *107*(B9), 2198 doi:10.1029/2000JB000093.

Norris, R. J., and A. F. Cooper (2001), Late Quaternary slip rates and slip partitioning on the Alpine Fault, New Zealand, *J. Structural Geol.*, *23*, 507–520, doi:10.1016/S0191-8141(00)00122-X.

Podolefsky, N. S., S. Zhong, and A. K. McNamara (2004), The anisotropic and rheological structure of the oceanic upper mantle from a simple model of plate shear, *Geophys. J. Int.*, *158*, 287–296, doi:10.1111/j.1365-246X.2004.02250.x.

Restivo, A., and G. Helffrich (1999), Teleseismic shear wave splitting measurements in noisy environments, *Geophys. J. Int.*, *137*, 821–830, doi:10.1046/j.1365-246x.1999.00845.x.

Ribe, N. M. (1992), On the relation between seismic anisotropy and finite strain, *J. Geophys. Res.*, *97*(B6), 8737–8747, doi:10.1029/92JB00551.

Rümpker, G., and T. Ryberg (2000), New "Fresnel-zone" estimates for shear-wave splitting observations from finite-difference modeling, *Geophys. Res. Lett.*, *27*(13), 2005–2008, doi:10.1029/2000GL011423.

Rychert, C. A., and P. M. Shearer (2009), A global view of the lithosphere-asthenosphere boundary, *Science*, *324*, 495–498, doi:10.1126/science.1169754.

Salmon, M., B. L. N. Kennett, T. Stern, and A. R. A. Aitken (2013), The Moho in Australia and New Zealand, *Tectonophysics*, *609*, 288–298, doi:10.1016/j.tecto.2012.07.009.

Savage, M. K. (1999), Seismic anisotropy and mantle deformation: What have we learned from shear wave splitting?, *Rev. Geophys.*, *37*(1), 65–106, doi:10.1029/98RG02075.

Savage, M. K., K. M. Fischer, and C. E. Hall (2004), Strain modelling, seismic anisotropy and coupling at strike-slip boundaries: Applications in New Zealand and the San Andreas Fault, in *Vertical Coupling and Decoupling in the Lithosphere*, vol. 227, edited by J. Grocott et al., pp. 9–39, Geol. Soc. Publishing House, Avon, U. K., doi:10.1144/GSL.SP.2004.227.01.02.

Savage, M. K., A. Tommasi, S. Ellis, and J. Chery (2007), Modeling strain and anisotropy along the Alpine fault, South Island, New Zealand, in *A Continental Plate Boundary: Tectonics at South Island, New Zealand*, Geophys. Monogr. Ser., vol. 175, edited by D. Okaya, T. Stern, and F. Davey, pp. 291–308, AGU, Washington, D. C., doi:10.1029/175GM15.

Scherwatch, M., T. A. Stern, A. Melhuish, and P. Molnar (2002), Pn anisotropy and distributed upper mantle deformation associated with a continental transform fault, *Geophys. Res. Lett.*, *29*, 16-1–16-4, doi:10.1029/2001GL014179.

Silver, P. G. (1996), Seismic anisotropy beneath the continents: Probing the depths of geology, *Annu. Rev. Earth Planet. Sci.*, *24*(1), 385–432.

Silver, P. G., and W. W. Chan (1991), Shear wave splitting and subcontinental mantle deformation, *J. Geophys. Res.*, *96*(B10), 16,429–16,454, doi:10.1029/91JB00899.

Silver, P. G., and M. K. Savage (1994), The interpretation of shear-wave splitting parameters in the presence of two anisotropic layers, *Geophys. J. Int.*, *119*, 949–963, doi:10.1111/j.1365-246X.1994.tb04027.x.

Skemer, P., J. M. Warren, P. B. Kelemen, and G. Hirth (2010), Microstructural and rheological evolution of a mantle shear zone, *J. Petrol.*, *51*, 43–53, doi:10.1093/petrology/egp057.

Skemer, P., J. M. Warren, and G. Hirth (2012), The influence of deformation history on the interpretation of seismic anisotropy, *Geochem. Geophys. Geosyst.*, *13*, Q03006, doi:10.1029/2011GC003988.

Skemer, P., J. M. Warren, L. N. Hansen, G. Hirth, and P. B. Kelemen (2013), The influence of water and LPO on the initiation and evolution of mantle shear zones, *Earth Planet. Sci. Lett.*, *375*, 222–233, doi:10.1016/j.epsl.2013.05.034.

Stachnik, J., A. F. Sheehan, D. W. Zietlow, Z. Yang, J. Collins, and A. Ferris (2012), Determination of New Zealand ocean bottom seismometer orientation via Rayleigh-wave orientation, *Seismol. Res. Lett.*, *83*, 704–713, doi:10.1785/0220110128.

Stern, T., P. Molnar, D. Okaya, and D. Eberhart-Phillips (2000), Teleseismic *P* wave delays and modes of shortening the mantle lithosphere beneath South Island, New Zealand, *J. Geophys. Res.*, *105*(B9), 21,615–21,631, doi:10.1029/2000JB900166.

Sutherland, R. (1999), Cenozoic bending of New Zealand basement terranes and Alpine Fault displacement: A brief review, *N. Z. J. Geol. Geophys.*, *42*, 295–301, doi:10.1080/00288306.1999.9514846.

Sutherland, R., F. Davey, and J. Beavan (2000), Plate boundary deformation in South Island, New Zealand, is related to inherited lithospheric structure, *Earth Planet. Sci. Lett.*, *177*, 141–151, doi:10.1016/S0012-821X(00)00043-1.

Turcotte, D. L., and G. Schubert (2002), *Geodynamics*, Cambridge Univ. Press, New York.

Vauchez, A., and A. Nicolas (1991), Mountain building: Strike-parallel motion and mantle anisotropy, *Tectonophysics*, *185*, 183–201, doi:10.1016/0040-1951(91)90443-V.

Walcott, R. I. (1998), Modes of oblique compression: Late Cenozoic tectonics of the South Island of New Zealand, *Rev. Geophys.*, *36*(1), 1–26, doi:10.1029/97RG03084.

Wallace, L. M., J. Beavan, R. McCaffrey, K. Berryman, and P. Denys (2007), Balancing the plate motion budget in the South Island, New Zealand using GPS, geological and seismological data, *Geophys. J. Int.*, *168*, 332–352, doi:10.1111/j.1365-246X.2006.03183.x.

Warren, J. M., G. Hirth, and P. B. Kelemen (2008), Evolution of olivine lattice preferred orientation during simple shear in the mantle, *Earth Planet. Sci. Lett.*, *272*, 501–512, doi:10.1016/j.epsl.2008.03.063.

Wessel, P., and W. H. F. Smith (1998), New, improved version of Generic Mapping Tools released, *Eos Trans. AGU*, *79*(47), doi:10.1029/98EO00426.

Wolfe, C. J., and P. G. Silver (1998), Seismic anisotropy of oceanic upper mantle: Shear wave splitting methodologies and observations, *J. Geophys. Res.*, *103*(B1), 749–771, doi:10.1029/97JB02023.

Wolfe, C. J., and S. C. Solomon (1998), Shear-wave splitting and implications for mantle flow beneath the MELT region of the East Pacific Rise, *Science*, *280*, 1230–1232, doi:10.1126/science.280.5367.1230.

Wüstefeld, A., and G. Bokelmann (2007), Null detection in shear-wave splitting measurements, *Bull. Seismol. Soc. Am.*, *97*, 1204–1211, doi:10.1785/0120060190.

Wüstefeld, A., G. Bokelmann, C. Zaroli, and G. Barruol (2008), SplitLab: A shear-wave splitting environment in Matlab, *Comput. Geosci.*, *34*, 515–528, doi:10.1016/j.cageo.2007.08.002.

Zhang, S., and S.-i. Karato (1995), Lattice preferred orientation of olivine aggregates deformed in simple shear, *Nature*, *375*, 774–777, doi:10.1038/375774a0.